MONTE CARLO MEAN FIELD TREATMENT OF MICROBUNCHING INSTABILITY IN THE FERMI@ELETTRA FIRST BUNCH COMPRESSOR

G. Bassi, University of Liverpool and Cockcroft Institute, Liverpool, UK *
J. A. Ellison, K. Heinemann, University of New Mexico, Albuquerque, NM, USA †
R. Warnock, SLAC National Accelerator Laboratory, Menlo Park, CA, USA ‡

INTRODUCTION

Bunch compressors, designed to increase the peak current, can lead to a microbunching instability with detrimental effects on the beam quality. This is a major concern for free electron lasers (FELs) where very bright electron beams are required, i.e. beams with low emittance and energy spread. In this paper, we apply our self-consistent, parallel solver to study the microbunching instability in the first bunch compressor system of FERMI@Elettra.

Our basic model is a 2D Vlasov-Maxwell system. We treat the beam evolution through a bunch compressor using our Monte Carlo mean field approximation. We randomly generate $\mathcal{N}$ points from an initial phase space density. We then calculate the charge density using a smooth density estimation procedure, from statistics, based on Fourier series. The electric and magnetic fields are calculated from the smooth charge/current density using a novel field formula that avoids singularities by using the retarded time as a variable of integration. The points are then moved forward in small time steps using the beam frame equations of motion, with the fields frozen during a time step, and a new charge density is determined using our density estimation procedure. We try to choose $\mathcal{N}$ large enough so that the charge density is a good approximation to the density that would be obtained from solving the 2D Vlasov-Maxwell system exactly. We call this method the Monte Carlo Particle (MCP) method. A detailed discussion can be found in [1].

A common approach to study the microbunching instability consists in calculating a gain factor for a given initial modulation wavenumber k_0 [2, 3]. The gain factor is defined as $\mid \tilde{\rho}(k_f, s_f)/\tilde{\rho}(k_0, 0) \mid$, where $\tilde{\rho}(k, s) = \int dz \exp(-ikz)\rho(z, s)$ and $k_f = C(s_f)k_0$ for a given initial wavelength of $\lambda_0 = 2\pi/k_0$. Here $\rho(z, s)$ is the longitudinal spatial density, $C(s) = 1/(1 + hR_{56}(s))$ is the compression factor of the chicane, s is arc length along the reference orbit, s_f is the value of s at exit of the chicane, and h is the chirp factor.

The function $\tilde{\rho}(k, s)$ is computed in our full nonlinear self-consistent scheme, but can also be approximated in some cases through a solution of the linearized Vlasov equation [1]. The linearized Vlasov solution can in turn be obtained as the solution of a 2D linear integral equation, provided that the collective force can be described by an impedance or equivalent wake field. The 2D integral equation reduces to the 1D integral equation of [2, 3] for the function $\tilde{\rho}(C(s)k_0, s)$ of s if the initial distribution describes a coasting beam with linear energy chirp.

Determining an approximate solution of the equation by iteration, Huang and Kim derived an analytic formula for the gain in [2, Eq. (38)].

We compare this gain formula with the gain from our full nonlinear MCP computation. We do this in the context of the spectrum $\tilde{\rho}(k, s)$ at $s = 0$ and s_f. Agreement is good at medium wavelengths, in spite of the fact that our collective force is computed in a more detailed way than that of [2], the latter being derived from the impedance for steady state coherent synchrotron radiation (CSR) without account of finite magnet length. At long wavelengths we begin to see the breakdown of the coasting beam assumption. At short wavelengths, as little as 40μm in calculations to date, there are deviations from the analytic gain formula. The source of discrepancy might be due to nonlinearity, or to the different models of the collective force, or both.

FERMI@ELETTRA BUNCH COMPRESSOR STUDIES

The FERMI@Elettra first bunch compressor system was proposed as a benchmark for testing codes [1]. The system consists of a 4-dipole chicane between rf cavities and quadrupoles. Here we limit our study to the chicane with parameters as listed in Table 1. The results are obtained in the free space case; i.e., neglecting shielding effects from the vacuum chamber. The lengths L_1, L_2 and L_b are in terms of the lab frame Z-variable, thus the total length of the chicane is 8m. The total arc length traversed by the reference particle is $s_f = 8.029$m.

Our initial beam frame phase space density is

$$f(z, p_z, x, p_x, 0) = (1 + \varepsilon(z))a_0(z, p_z, x, p_x) \ , \quad (1)$$

where

$$a_0(z, p_z, x, p_x) = \mu(z)\rho_c(p_z - hz)$$

* gabriele.bassi@stfc.ac.uk
† Work supported by US DOE grant DE-FG02-99ER41104
‡ Work supported by US DOE grant DE-AC02-76SF00515

Table 1: Chicane Parameters and Beam Parameters at First Dipole

Parameter	Symbol	Value	Unit
Energy reference particle	E_r	233	MeV
Peak current	I	120	A
Bunch charge	Q	1	nC
Norm. transverse emittance	$\gamma\epsilon_0$	1	μm
Alpha function	α_0	0	
Beta function	β_0	10	m
Linear energy chirp	h	-12.6	1/m
Uncorrelated energy spread	σ_E	2	KeV
Momentum compaction	R_{56}	0.057	m
Radius of curvature	r_0	5	m
Magnetic length	L_b	0.5	m
Dist. 1st-2nd, 3rd-4th bend	L_1	2.5	m
Dist. 2rd-3nd bend	L_2	1	m

$$\begin{aligned}
&\times \exp[-(x^2 + (\alpha_0 x + \beta_0 p_x)^2)/2\epsilon_0\beta_0]/2\pi\epsilon_0 \ , \\
&\rho_c(p_z) = \exp[-p_z^2/2\sigma_u]/\sqrt{2\pi}\sigma_u \ , \\
&\mu(z) = [\tanh((z+a)/b) - \tanh((z-a)/b)]/4a \ , \\
&\varepsilon(z) = A\cos(2\pi z/\lambda_0) = A\cos(k_0 z) \ . \qquad (2)
\end{aligned}$$

Here h is the linear chirp parameter and μ is a smooth flat-top density of width $\approx 2a$. Thus the smooth a_0 is perturbed by a modulation, ε, with wavelength λ_0 and small amplitude A. In the calculations we fix $A = .05$, $a = 1180\mu$m and $b = 150\mu$m and vary λ_0.

An important part of our current calculation is that we have found an s-independent grid for the spatial density that allows us to minimize the number of grid points. The spatial density is stationary in this grid for $\sigma_u = \sigma_{p_{x0}} = 0$ and no self forces.

We calculate the evolution of the 2D spatial density given the initial beam frame phase space density of Eq. (1). In Fig. 1 (right) we show the initial longitudinal density for $\lambda_0 = 100\mu$m. We present results for several perturbation wavelengths λ_0. We present results for the 2D spatial density but our main focus will be on the longitudinal density $\rho(z, s)$ and its Fourier transform $\tilde{\rho}(k, s)$. In particular, we calculate the gain factor $\mid \tilde{\rho}(k_f, s_f)/\tilde{\rho}(k_0, 0) \mid$ for an initial modulation of wavelength $\lambda_0 = 2\pi/k_0 \geq 40\mu$m and present spectra $\tilde{\rho}(k, s_f)$ for several λ_0.

In Fig. 1 (left) we compare the analytical gain factor given in [2], with the gain factor calculated numerically with our solver (red squares). The formula from [2] takes into account only CSR effects whereas our Vlasov-Maxwell approach automatically includes the effects of CSR and space charge. Because our approach is much more detailed than the analytic approach we did not expect detailed agreement. Nonetheless, there does seem to be rough agreement in the $100 - 450\mu$m range. To gain some understanding we consider the full spectra. Spectra for $\lambda_0 = 300\mu$m are shown in Fig. 2. In Fig. 2 (left) we show the initial, $s = 0$, spectra for unperturbed ($A = 0$) and perturbed ($A = 0.05$) distribution. We note that two spectra are essentially the same until $k \approx$ 19,000. After this the unperturbed spectrum is essentially zero whereas the perturbed spectrum has a substantial contribution in a neighborhood of the perturbed wavenumber k_0 =20,944. We note however that the peak is at a slightly larger k value. We see a similar structure for the evolved spectra at $s = s_f$ in Fig. 2 (center). The two spectra are the same until $k \approx$ 60,000. After this the unperturbed spectrum is ≈ 0 and the perturbed spectrum has a substantial contribution in a neighbourhood of the perturbed but amplified wavenumber $C(s_f)k_0$ =74,247 ($C(s_f) = 3.54$). The amplified wavenumber is slightly to the left of the peak. This raises the issue of how the gain should be defined from the spectrum. One possibility would be to take the ratio of the peak values. Fig. 1 (left) shows the ratio of the peak values (blue dots) as well as the ratio of the values at k_0 and $k_0 C(s_f)$. Perhaps a better approach would be to consider some integral of the spectrum.

The spectra for $\lambda_0 = 100\mu$m are shown in Fig. 2 (right). Here we see considerable enhancement and structure at the end of the chicane near the amplified k_0. Perhaps defining the gain as the ratio of the values at the arrows misses the mark in two ways. The arrow at $s = s_f$ is to the right of the peak and it does not take into account the considerable structure between 200,000 and 250,000.

At 80μm it appears that our calculation shows a decrease in the gain as indicated by the red squares and blue dots of Fig. 1 (left). However, this may be misleading as a comparison of the spectra at 80μm, Fig. 3 (left), and $\lambda_0 = 100\mu$m, Fig. 2 (right), shows.

At 60μm, Fig. 3 (center), the situation is similar to the 80μm case.

At 40μm the amplification of the initial modulation decreases as indicated by the spectra in Fig. 3 (right) and by the longitudinal density in Fig. 5 (right).

Our goal is to go down in λ_0 as far as possible and we have made an important advance in this direction with our new stationary grid. Currently we are running on Encanto at the New Mexico Computing Applications Center (NMCAC) and on Franklin at the National Energy Research Scientific Computing Center (NERSC). Our run at 40μm takes ≈ 5 hours using 800 processors. This, along with memory considerations, currently limits the minimum value of λ_0 we can study.

We have also studied the spectra for values of λ_0 greater than 300μm. At $\lambda_0 = 400\mu$m we begin to see an overlap between the perturbed and unperturbed spectra and the arrows are quite a bit to the left of the peak values. This is the beginning of the break down of the coasting beam assumption, where there are only few of oscillations on the flattop. The overlap is illustrated at 600μm in Fig. 4 (left and center frames). In Fig. 1 (left) we see that at 400μm the red and blue markers are very close and at 600μm the blue marker is almost on the analytic curve, but these are likely fortuitous results.

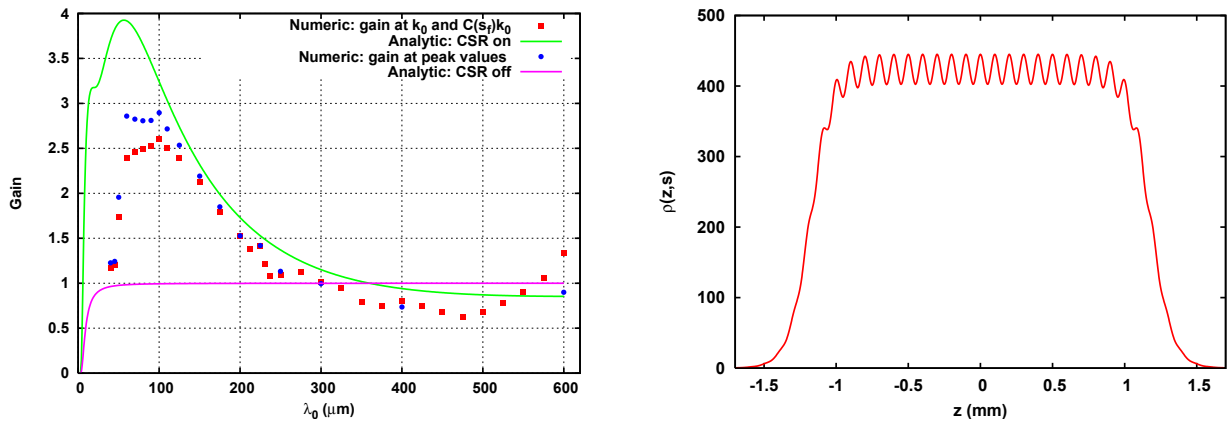

Figure 1: Left: gain factor from analytical formula in [2] (curves) and from our Vlasov solver (red squares and blue dots). The numerical gain is calculated as the ratio of the values of the spectrum at k_0 and $k_0 C(s_f)$ (red squares) and as the ratio of the peak values of the spectrum (blue dots). Right: longitudinal spatial density at $s = 0$ for an initial modulation $\lambda_0 = 100\mu$m.

The effect of the modulation on the average longitudinal force (mean power) and on the transverse emittance is very small for all values of λ_0, details are in [1].

In Fig. 4 (right) and Fig. 5 we show the longitudinal density for $\lambda_0 = 100$, 80, 60 and 40μm. As already shown in the discussion of the spectra, an amplification of the initial modulation of $A = 0.05$ is clearly visible. We note that the amplification is roughly constant for $\lambda_0 = 100$, 80 and 60μm, and decreases at 40μm.

In Fig. 6 and Fig. 7 (left) we show the 2D spatial density at s_f for $\lambda_0 = 200$, 100 and 80μm. In Fig. 7 (right) and Fig. 8 we show the longitudinal force, which is proportional to $\mathbf{E} \cdot \mathbf{t}$, at $s = 8.029$m for $\lambda_0 = 200$, 100 and 80μm. Notice that the longitudinal force is amplified accordingly to the microbunching structure in the 2D spatial density.

OUTLOOK AND FUTURE WORK

The study of the gain factor at short wavelengths is computationally expensive. Moreover, the increased length of the 3D arrays needed to store the history of the charge/current densities leads to intensive memory usage. We are attempting to improve the Monte Carlo integrations by trying variance reduction techniques, which build on the central limit theorem, and also by trying quasi-random sequences (also called low-discrepancy sequences) in place of pseudo-random sequences. Quasi-random sequences allow one to break the "curse of dimensionality" in grid-based multi-dimensional integration, giving a true error bound (i.e., not probabilistic) of order $(\log \mathcal{N})^{k-1}/\mathcal{N}$, with only logarithmic dependence on the dimension k of the space [1].

As an alternative to MCP, where the Fourier coefficients are calculated with Monte Carlo integrations, we are investigating a much faster scheme based on the standard PIC procedure of charge deposition to a grid, where the Fourier coefficients are calculated with quadratures. A comparison of this method with a standard filtering method based on wavelets is discussed in [4]. We are also pursuing kernel density estimation methods from statistics. These are closely related to quasi-interpolation methods from scattered data approximation [1].

Other improvements on our agenda are a different choice of integration variables for the field calculation and the optimization of the algorithm to fix the relevant support of the integrand in the field formula.

Studies are in progress to investigate wavelengths shorter than $\lambda_0 = 40\mu$m and different amplitudes A. An important prediction of the gain factor formula from [2] is that increasing the uncorrelated energy spread reduces the gain factor. This led to a proposal, the laser heater, to increase the uncorrelated energy spread within FEL tolerance in order to damp the microbunching instability without degrading the FEL performance. An analysis of this effect together with the complete study of the FERMI@Elettra benchmark bunch compressor system will be discussed in a forthcoming paper.

ACKNOWLEDGMENTS

We gratefully acknowledge T. Thomas at the University of New Mexico HPC, and R. Ryne and P. Spentzouris for an account on NERSC.

REFERENCES

[1] G. Bassi, J. A. Ellison, K. Heinemann and R. Warnock, submitted to PRSTAB.

[2] H. Huang and K. Kim, Phys. Rev. ST-AB **5**, 074401 and 129903 (2002).

[3] S. Heifets, G. Stupakov and S. Krinsky, Phys. Rev. ST-AB **5**, 064401 (2002).

[4] G. Bassi and B. Terzic. These Proceedings, paper TH5PFP043.

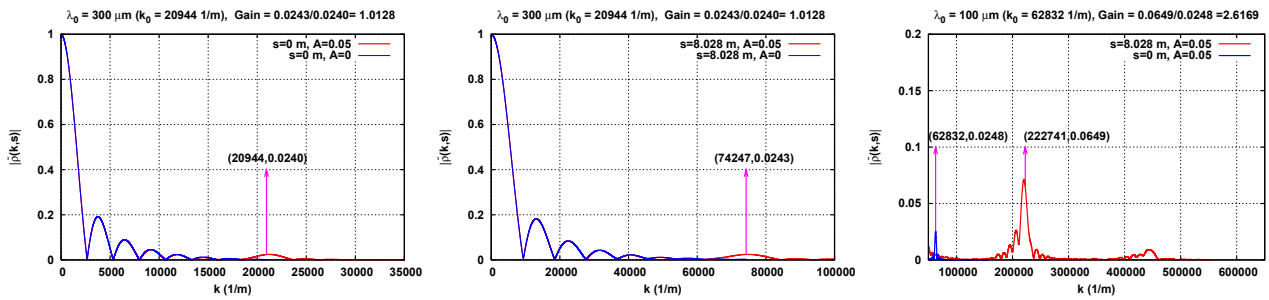

Figure 2: Left: spectra for $\lambda_0 = 300\mu$m with and without perturbation at $s = 0$. Center: spectra for $\lambda_0 = 300\mu$m with and without perturbation at $s = s_f$. Right: spectra at $s = 0$ and $s = s_f$ for $\lambda_0 = 100\mu$m.

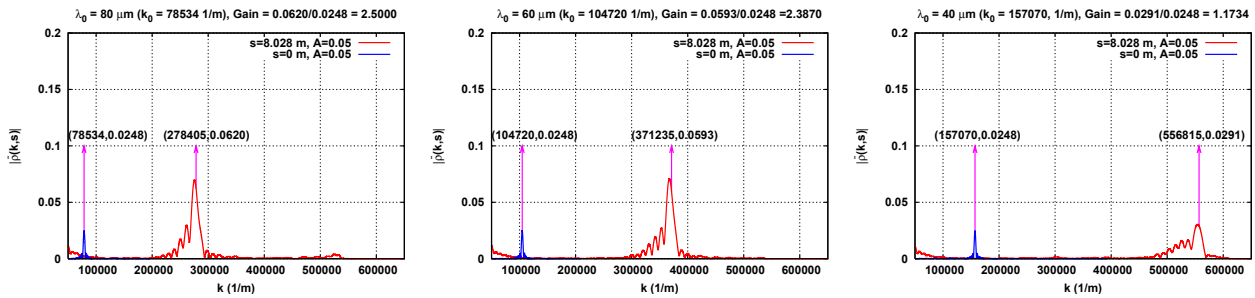

Figure 3: Spectra at $s = 0$m and $s = s_f$, for $\lambda_0 = 80\mu$m (left) and $\lambda_0 = 60\mu$m (center) and $\lambda_0 = 40\mu$m (right).

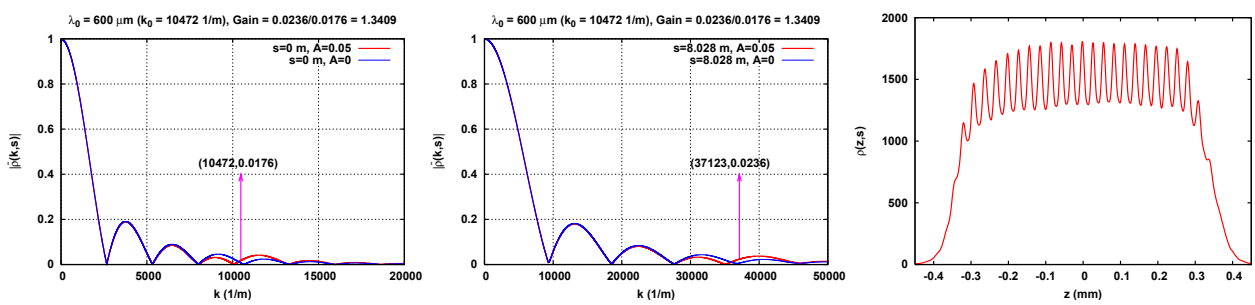

Figure 4: Left: spectra for $\lambda_0 = 600\mu$m with and without perturbation at $s = 0$. Center: spectra for $\lambda_0 = 600\mu$m with and without perturbation at $s = s_f$. Right: longitudinal density at $s = s_f$ for $\lambda_0 = 100\mu$m.

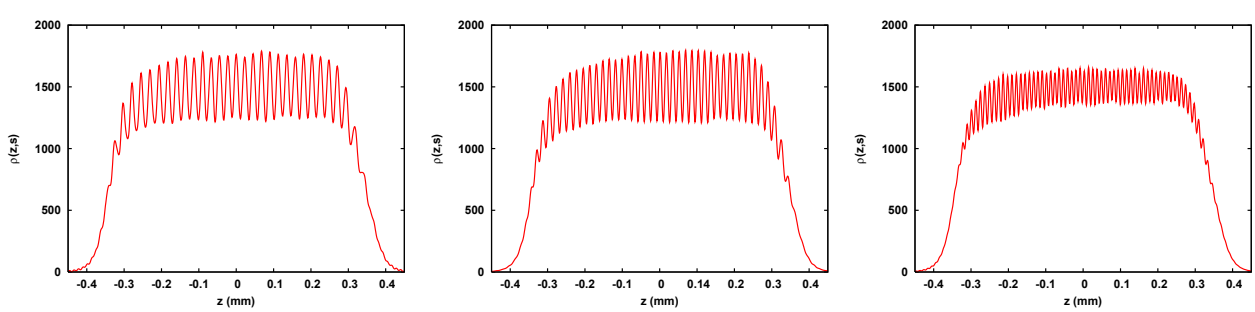

Figure 5: Longitudinal density at $s = s_f$ for $\lambda_0 = 80\mu$m (left), $\lambda_0 = 60\mu$m (center) and $\lambda_0 = 40\mu$m (right).

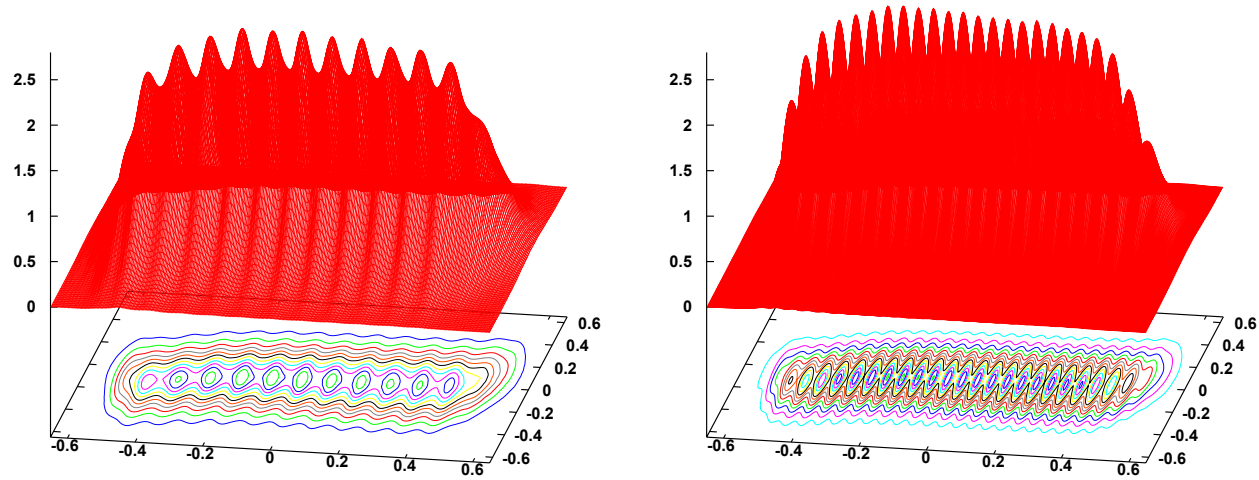

Figure 6: 2D spatial density in grid coordinates at $s = s_f$ for $\lambda_0 = 200\mu$m (left) and $\lambda_0 = 100\mu$m (right).

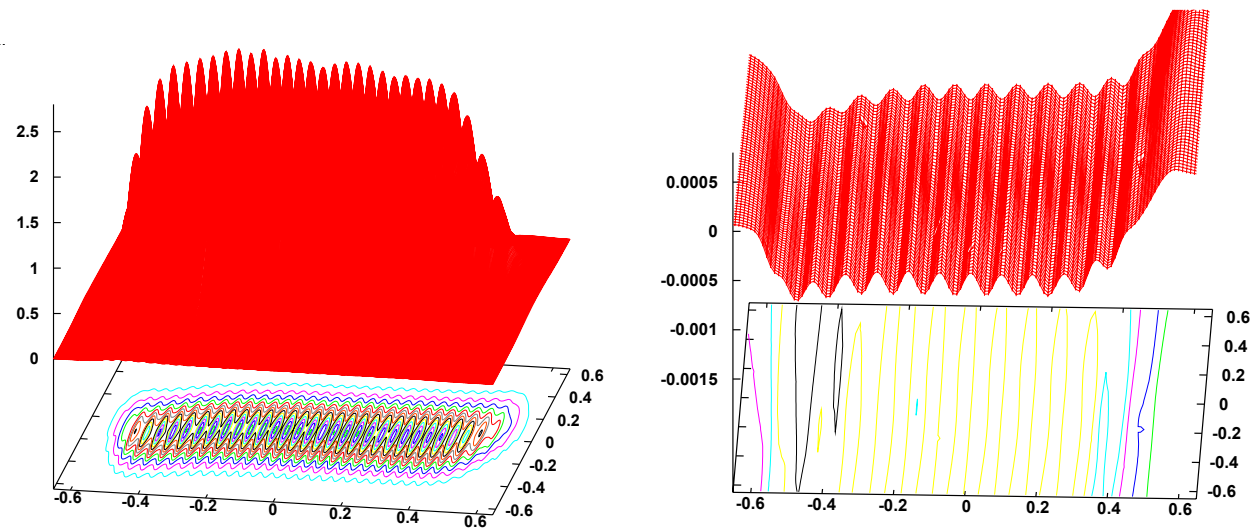

Figure 7: Left: 2D spatial density at $s = s_f$ for $\lambda_0 = 80\mu$m in grid coordinates. Right: longitudinal force in grid coordinates at $s = s_f$ for $\lambda = 200\mu$m.

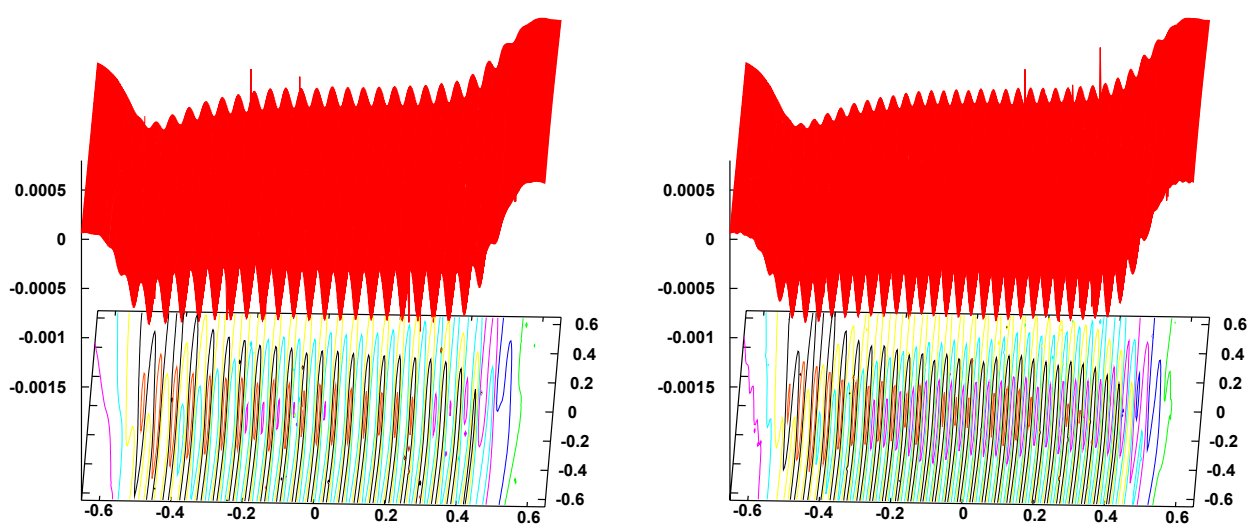

Figure 8: Longitudinal force in grid coordinates at $s = s_f$ for $\lambda_0 = 100\mu$m (left) and $\lambda_0 = 80\mu$m (right).